5154 *Chem. Mater.* **2010,** *22,* 5154–5164
DOI:10.1021/cm1009493

CHEMISTRY OF MATERIALS
Article

In Situ Catalytic Encapsulation of Core-Shell Nanoparticles Having Variable Shell Thickness: Dielectric and Energy Storage Properties of High-Permittivity Metal Oxide Nanocomposites

Zhong Li,[†] Lisa A. Fredin,[†] Pratyush Tewari,[‡] Sara A. DiBenedetto,[†] Michael T. Lanagan,*[,‡] Mark A. Ratner,*[,†] and Tobin J. Marks*[,†]

[†]*Department of Chemistry and the Materials Research Center, Northwestern University, Evanston, Illinois 60208-3113, and* [‡]*Center for Dielectric Studies, Materials Research Institute, The Pennsylvania State University, University Park, Pennsylvania 16802-4800*

Received April 5, 2010. Revised Manuscript Received July 14, 2010

Aluminum oxide encapsulated high-permittivity (ε) $BaTiO_3$ and ZrO_2 core-shell nanoparticles having variable Al_2O_3 shell thicknesses were prepared via a layer-by-layer methylaluminoxane coating process. Subsequent chemisorptive activation of the single-site metallocene catalyst [*rac*-ethylene-bisindenyl]zirconium dichloride ($EBIZrCl_2$) on these Al_2O_3-encapsulated nanoparticles, followed by propylene addition, affords 0−3 metal oxide-isotactic polypropylene nanocomposites. Nanocomposite microstructure is analyzed by X-ray diffraction, transmission electron microscopy, scanning electron microscopy, differential scanning calorimetry, atomic force microscopy, and Raman spectroscopy. The in situ polymerization process yields homogeneously dispersed nanoparticles in a polyolefin matrix. Electrical measurements indicate that as the concentration of the filler nanoparticles increases, the effective permittivity of the nanocomposites increases, affording ε values as high as 6.2. The effective permittivites of such composites can be predicted by the Maxwell−Garnett formalism using the effective medium theory for volume fractions (v_f) of nanoparticles below 0.06. The nanocomposites have leakage current densities of $\sim 10^{-7}-10^{-9}$ A/cm^2 at an electric field of 10^5 V/cm, and very low dielectric loss in the frequency range 100 Hz−1 MHz. Increasing the Al_2O_3 shell thickness dramatically suppresses the leakage current and high field dielectric loss in these nanocomposites.

Introduction

Materials having high dielectric permittivity, high breakdown strength, low loss, and fast response will be essential for next-generation electrical and electronic applications,[1] such as high energy density pulsed-power and power capacitors.[2] Conventional ceramic dielectrics have high permittivities and low working voltages; however, they are difficult to process into multilayer thin films and require high temperature sintering.[3] Polymer dielectrics, for example isotactic polypropylene, which is widely used in power capacitors, have good dielectric strength and facile processability, but their low dielectric permittivities limit their applications.[4] Recently, inorganic−polymer nanocomposite materials have attracted great attention because they offer the possibility of combining the best properties of both phases, yielding potential performance well beyond that of each individual constituent material.[5] For example, by dispersing high permittivity inorganic nanoparticles in polymer matrices, some 0−3 composites (zero-dimensional structure, i.e., spheres in a three-dimensional matrix) have afforded processable materials with permittivies approaching 50.[6]

Inorganic−polymer 0−3 nanocomposite syntheses employing conventional solution mixing[7] or mechanical

(1) (a) Pan, J.; Li, K.; Li, J.; Hsu, T.; Wang, Q. *Appl. Phys. Lett.* **2009**, *95*, 022902. (b) Claude, J.; Lu, Y.; Li, K.; Wang, Q. *Chem. Mater.* **2008**, *20*, 2078–2080. (c) Cao, Y.; Irwin, P. C.; Younsi, K. *IEEE Trans. Dielectr. Electr. Insul.* **2004**, *11*, 797–807. (d) Nalwa, H. S., Ed.; *Handbook of Low and High Dielectric Constant Materials and their Applications*; Academic Press: New York, 1999; Vol. *2*.

(2) (a) Mackey, M.; Hiltner, A.; Baer, E.; Flandin, L.; Wolak, M. A.; Shirk, J. S. *J. Phys. D: Appl. Phys.* **2009**, *42*, 175304. (b) Han, Y. X.; Lin, F.; Dai, L.; Li, H.; Wang, L.; Bo, L.; Long, Z. Z.; Peng, B. *IEEE Trans. Dielectr. Electr. Insul.* **2009**, *16*, 979–984. (c) Wallace, R. M.; Wilk, G. D. *Crit. Rev. Solid State* **2003**, *28*, 231–285. (d) Slenes, K. M.; Winsor, P.; Scholz, T.; Hudis, M. *IEEE Trans. Magn.* **2001**, *37*, 324–327.

(3) Polotai, A. V.; Yang, G. Y.; Dickey, E. C.; Randall, C. A. *J. Am. Ceram. Soc.* **2007**, *90*, 3811–3817.

(4) (a) Michalczyk, P.; Bramoulle, M. *IEEE Trans. Magn.* **2003**, *39*, 362–365. (b) Rabuffi, M.; Picci, G. *IEEE Trans. Plasma Sci.* **2002**, *30*, 1939–1942.

(5) (a) Kim, P.; Doss, N. M.; Tillotson, J. P.; Hotchkiss, P. J.; Pan, M.-J.; Marder, S. R.; Li, J.; Calame, J. P.; Perry, J. W. *ACS Nano* **2009**, *3*, 2581–2592. (b) Li, J.; Seok, S. I.; Chu, B.; Dogan, F.; Zhang, Q.; Wang, Q. *Adv. Mater.* **2009**, *21*, 217–221. (c) Li, J.; Claude, J.; Norena-Franco, L. E.; Selk, S.; Wang, Q. *Chem. Mater.* **2008**, *20*, 6304–6306. (d) Gross, S.; Camozzo, D.; Di Noto, V.; Armelao, L.; Tondello, E. *Eur. Polym. J.* **2007**, *43*, 673–696. (e) Tanaka, T.; Montanari, G. C.; Mulhaupt, R. *IEEE Trans. Dielectr. Electr. Insul.* **2004**, *11*, 763–784.

(6) (a) Qi, L.; Lee, B. I.; Chen, S.; Samuel, W. D.; Exarhos, G. J. *Adv. Mater.* **2005**, *17*, 1777–1781. (b) Bai, Y.; Chen, Z. Y.; Bharti, V.; Xu, H. S.; Zhang, Q. M. *App. Phys. Lett.* **2000**, *76*, 3804–3806.

(7) (a) Kobayashi, Y.; Tanase, T.; Tabata, T.; Miwa, T.; Konno, M. *J. Eur. Ceram. Soc.* **2008**, *28*, 117–122. (b) Dhang, Z. M.; Xu, H. B.; Wang, H. Y. *App. Phys. Lett.* **2007**, *90*, 012901. (c) Schroeder, R.; Majewski, L.; Grell, M. *Adv. Mater.* **2005**, *17*, 1535–1539.

Published on Web 08/31/2010

Scheme 1

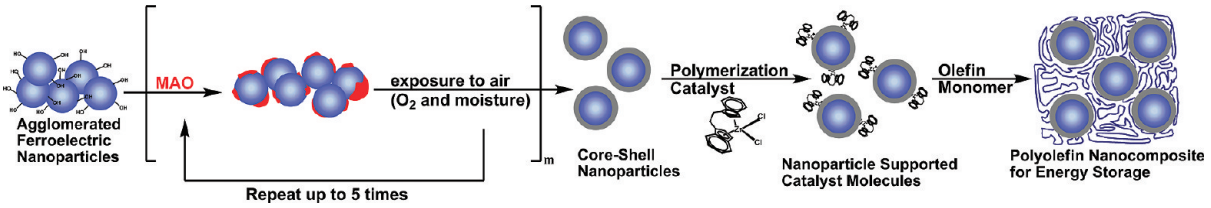

blending methods[8] frequently yield agglomerated nanoparticles, voids, and phase-separated mixtures. Consequently, such inhomogeneous films lead to high dielectric loss and low dielectric strength. While surfactant addition during nanocomposite processing[9] and covalent grafting of polymer chains to inorganic nanoparticles,[10] have in some instances increased the nanoparticle dispersion in the host polymer, a completely different approach, in situ polymerization, affords a simpler, effective, cost-effective, and void-free means of dispersing the particles.[11]

Previously, we reported an efficient method for the in situ synthesis of polyolefin-based nanocomposite dielectric materials by chemisorbing the types of metallocene olefin polymerization catalysts that are used commercially to produce polyolefins on a huge scale, on high-ε oxide nanoparticle surfaces (Scheme 1).[11] This concept is inspired by the SiO_2 catalyst supports used in large-scale heterogeneous or slurry olefin polymerizations, where the substantial local hydraulic pressures arising from the propagating polyolefin chains result in extensive SiO_2 particle fracture.[12−14] In a similar way, in situ polymerization mediated by metallocenes supported on oxide nanoparticles has been shown to disrupt nanoparticle agglomeration.[15] The resulting 0−3 nanocomposites prepared from high-ε $BaTiO_3$, TiO_2, ZrO_2, and yttria-stabilized zirconia nanoparticle fillers dispersed in polyolefins (polypropylene, polyethylene, polystyrene, and other copolymers) exhibit both high effective permittivities, high dielectric breakdown metrics, and very good energy storage capacities.[15]

Chart 1

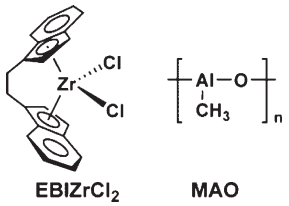

Generally, to achieve high effective composite permittivity and energy density, the filler must have a much greater permittivity than the surrounding polymer matrix.[16] However, a high dielectric contrast in permittivity between two phases leads to a highly inhomogeneous electric fields and poor dielectric properties.[17] Note that for nanocomposite materials, the interfacial regions between the inorganic filler and polymer matrix can have profound effects on the dielectric properties, and a variety of coupling agents have been used to modify the interfacial modulus.[9,18] In this regard, Tanaka and co-workers proposed a multicore model composed of a bonded layer, a bound layer, and a loose layer to describe the interactions of the components in a polymer nanocomposite dielectric.[19] In the present case, an Al_2O_3 layer formed by ambient exposure of the methylalumoxane (MAO) cocatalyst/activator coating (Chart 1) is interposed between the nanoparticle and the polymer matrix. Note that this Al_2O_3 layer has moderate dielectric permittivity ($\varepsilon \sim 10$) and therefore acts as a buffer layer between the high-ε nanoparticle ($\varepsilon \sim 50-2000$) and the polyolefin ($\varepsilon \sim 2.25$) components, which would otherwise have a very large permittivity contrast.

In the present contribution, we synthesize $BaTiO_3$ and ZrO_2 nanoparticles encapsulated by varying Al_2O_3 shell

(8) (a) Dang, Z. M.; Lin, Y. H.; Nan, C. W. *Adv. Mater.* **2003**, *15*, 1625–1629. (b) Dang, Z.; Wu, J.; Fan, L.; Nan, C. *Chem. Phys. Lett.* **2003**, *376*, 389–394.
(9) (a) Kim, P.; Jones, S. C.; Hotchkiss, P. J.; Haddock, J. N.; Kippelen, B.; Marder, S. R.; Perry, J. W. *Adv. Mater.* **2007**, *19*, 1001–1005. (b) Ramesh, S.; Shutzberg, B. A.; Huang, C.; Gao, J.; Giannelis, E. P. *IEEE Trans. Adv. Packaging* **2003**, *16*, 17–24.
(10) Roy, M.; Nelson, J. K.; McCrone, R. K.; Schadler, L. S.; Reed, C. W.; Keefe, R.; Zeneger, W. *IEEE Trans. Dielectr. Electr. Insul.* **2005**, *12*, 629–643.
(11) (a) Guo, N.; DiBenedetto, S. A.; Kwon, D. K.; Wang, L.; Russell, M. T.; Lanagan, M. T.; Facchetti, A.; Marks, T. J. *J. Am. Chem. Soc.* **2007**, *129*, 766–767.
(12) (a) Kaminsky, W.; Funck, A.; Wiemann, K. *Macromol. Symp.* **2006**, *239*, 1–6. (b) Li, K.-T.; Kao, Y.-T. *J. Appl. Polym. Sci.* **2006**, *101*, 2573–2580. (c) Fink, G.; Steinmetz, B.; Zechlin, J.; Przybyla, C.; Tesche, B. *Chem. Rev.* **2000**, *100*, 1377–1390.
(13) For recent reviews of single-site olefin polymerization, see: (a) Amin, S. B.; Marks, T. J. *Angew. Chem., Int. Ed.* **2008**, *47*, 2006–2025. (b) Marks, T. J., Ed.; Proc. Natl. Acad. Sci. U.S.A., **2006**, *103*, 15288−15354, and contributions therein (special feature on polymerization). (c) Suzuki, N. *Top. Organomet. Chem.* **2005**, *8*, 177–216. (d) Alt, H. G. *Dalton Trans.* **2005**, *20*, 3271–3276. (e) Kaminsky, W. *J. Polym. Sci., Polym. Chem.* **2004**, *42*, 3911–3921. Wang, W.; Wang, L. *J. Polym. Mater.* **2003**, *20*, 1–8. (f) Delacroix, O.; Gladysz, J. A. *Chem. Commun.* **2003**, *6*, 665–675. (g) Kaminsky, W.; Arndt-Rosenau, M. *Applied Homogeneous Catalysis with Organometallic Compounds*, 2nd ed.; Wiley-VCH Verlag GmbH: Weinheim, Germany, 2002 (h) Lin, S.; Waymouth, R. M. *Acc. Chem. Res.* **2002**, *35*, 765–773. (i) Chen, E. Y.-X.; Marks, T. J. *Chem. Rev.* **2000**, *100*, 1391–1434.
(14) For recent discussions of single-site heterogeneous polymerization catalysis, see: (a) Williams, L. A.; Marks, T. J. *Organometallics* **2009**, *28*, 2053–2061, and the references therein. (b) Copéret, C.; Chabanas, R.; Petroff Saint-Arroman, R.; Basset, J.-M. *Angew. Chem., Int. Ed.* **2003**, *42*, 156–181. (c) Hlatky, G. G. *Chem. Rev.* **2000**, *100*, 1347–1376. (d) Reven, L. *J. Mol. Catal.* **1994**, *86*, 447–477. (e) Marks, T. J. *Acc. Chem. Res.* **1992**, *25*, 57.
(15) Guo, N.; DiBenedetto, S. A.; Tewari, P.; Lanagan, M. T.; Ratner, M. A.; Marks, T. J. *Chem. Mater.* **2010**, *22*, 1567–1578.
(16) An, L.; Boggs, S. A.; Calame, J. P. *IEEE Electr. Insul. Mag.* **2008**, *24*, 5–10.
(17) Li, J. Y.; Zhang, L.; Duchame, S. *Appl. Phys. Lett.* **2007**, *90*, 132901.
(18) (a) Kim, P.; Doss, N. M.; Tillotson, J. P.; Pan, M.-J.; Marder, S. R.; Li, J.; Calame, J. P.; Perry, J. W. *ACS Nano* **2009**, *3*, 2581–2592. (b) Li, J.; Claude, J.; Norena-Franco, L. E.; Selk, S.; Wang, Q. *Chem. Mater.* **2008**, *20*, 6304–6306. (c) Lewis, T. J. *IEEE Trans. Dielectr. Electr. Insul.* **2004**, *11*, 739–753.
(19) Tanaka, T.; Kozako, M.; Fuse, N.; Ohiki, N. *IEEE Trans. Dielectr. Electr. Insul.* **2005**, *12*, 669–681.

thicknesses via layer-by-layer MAO coating of the nanoparticle surface. The MAO-coated core-shell nanoparticles then bind and activate a metallocene precatalyst, [*rac*-ethylenebisindenyl]zirconium dichloride ($EBIZrCl_2$, Chart 1), for the in situ synthesis of highly isotatic polypropylene. The microstructures of these nanocomposites are characterized by X-ray diffraction (XRD) as well as by transmission electron microscopy (TEM), scanning electron microscopy (SEM), differential scanning calorimetry (DSC), atomic force microscopy (AFM), and Raman spectroscopy. Capacitors are then fabricated from these materials and are characterized experimentally by a full range of electrical measurements, and theoretically using effective medium theory. It will be seen that the thickness of the Al_2O_3 coating has little effect on the nanocomposite dielectric permittivity but dramatically lowers the leakage current density and dielectric loss.

Experimental Section

Materials and Methods. All manipulations of air-sensitive materials were performed with rigorous exclusion of oxygen and moisture using Schlenk techniques, or interfacing equipment to a high-vacuum line (10^{-6} Torr), or in a N_2-filled MBraun glovebox with a high capacity recirculator (<1 ppm O_2 and H_2O). Propylene (Matheson, polymerization grade) was purified by passage through a supported MnO O_2-removal column and an activated Davison 4 Å molecular sieve column. Toluene was dried using an activated alumina column and Q-5 columns, and then vacuum-transferred from Na/K alloy and stored in Teflon-valve sealed bulbs.[20] $BaTiO_3$ (d = 100−200 nm) and ZrO_2 (d = 50−100 nm) nanoparticles were purchased from Sakai Chemical and Sigma-Aldrich, respectively. Since it is known that $BaTiO_3$ surfaces often contain some $BaCO_3$ after exposure to aqueous atmosphere,[21] the $BaTiO_3$ nanoparticles were washed with dilute aqueous HCl acid, deionized water, and acetone before use to limit this contamination. The $BaTiO_3$ and ZrO_2 nanoparticles were then dried on a high vacuum line (10^{-5} Torr) at 80 °C overnight to remove any surface-bound water. The reagent [*rac*-ethylenebisindenyl]zirconium dichloride was purchased from Sigma-Aldrich and used as received. Methylaluminoxane, 10% solution in toluene, was purchased from Sigma-Aldrich and purified by removing all the volatiles in vacuo. Aluminum substrates were purchased from McMaster−Carr (Chicago, IL) and cleaned according to standard procedures.[22]

Physical and Analytical Measurements. Elemental analyses were performed by Midwest Microlabs, LLC, Indianapolis, IN. Inductively coupled plasma-optical emission spectroscopy (ICP-OES) analyses were performed by Galbraith Laboratories, Inc., Knoxville, Tennessee. Powder XRD data were recorded on a Rigaku DMAX-A diffractometer with Ni-filtered Cu Kα radiation (1.54184 Å). TEM was performed on a Hitachi H-8100 TEM with an accelerating voltage of 200 kV. Composite thermal transitions were measured on a TA Instruments 2920 temperature modulated differential scanning calorimeter. Typically, about 6 mg of sample was examined, and a ramp rate of 10 °C/min was used to measure the melting point. To erase thermal history effects, all samples were subjected to two melt-freeze cycles; only data from the second melt-freeze cycle are presented.

The nanocomposite dielectric films were fabricated on Al substrates by hot pressing at 130 °C and 1500 psi pressure. Post-pressing vacuum treatment at 80 °C was performed on all samples overnight to remove any residual moisture and trapped air bubbles. Parallel-plate capacitors were fabricated by vapor-depositing gold electrodes on the dielectric nanocomposite films (see more below). The thicknesses of the films were measured on a Tencor P-10 step profilometer and used to calculate the dielectric permittivity. The film morphologies were also examined with a LEO1525 scanning electron microscope under an accelerating voltage of 3 kV after coating with 6 nm osmium using an SPF osmium coater. Film topography and rms roughnesses were imaged using a NIFTI JEOL SPM atomic force microscope. The UV Raman spectra were measured using a locally constructed UV Raman instrument. Details of the UV Raman instrument are provided elsewhere.[23] The Raman spectra were excited at 244 nm generated by an intracavity, frequency-doubled argon ion laser (Lexel 95 SHG). The laser power at the sample is 4 mW, and a typical spectrum collection time is 20 min. The UV Raman spectra were recorded in air.

Electrical Measurements. Gold electrodes for metal−insulator−metal (MIM) devices were vacuum-deposited through shadow masks at (3−4) × 10^{-7} Torr (500 Å, 0.2−0.5 Å/s). A digital capacitance meter (Model 3000, GLK Instruments, San Diego CA) was used for capacitance measurements. Frequency-dependent (100−1 M Hz) capacitance and loss tangent were measured on an HP 4384A precision or an Agilent E4980A LCR meter. Leakage current measurements were performed using a Keithley 6430 sub-femtoamp remote source meter using a locally written LABVIEW program. All of the above electrical characterizations were performed under ambient conditions in air.

Preparation of Al_2O_3-Encapsulated $BaTiO_3$ and ZrO_2 Nanoparticles. In the glovebox, 2.0 g of $BaTiO_3$ or ZrO_2 nanoparticles, 200 mg of MAO, and 50 mL of dry toluene were loaded into a predried 200 mL flip-frit reaction flask. The mixture was subjected to alternating sonication and vigorous stirring for 1 day with constant removal of evolving methane. Then the nanoparticles were collected by filtration and washed with fresh toluene (50 mL × 4) to remove any residual MAO. This procedure produces one monolayer of MAO coated on the surface of the nanoparticles. After brief drying under vacuum, the particles were next exposed to air and stirred at room temperature for 3 h, and then dried under vacuum at 80 °C overnight. The MAO coating is oxidized and hydrolyzed in this procedure to form a layer of amorphous Al_2O_3.[11,15] The flask was next transferred to the glovebox, 200 mg of MAO and 50 mL of dry toluene were added again, and the sonication and reaction processes repeated to deposit another monolayer of MAO. This process was repeated up to five times in this study. In the final cycle, after rinsing off the excess MAO, the particles were dried under vacuum at room temperature overnight and stored in glovebox at −40 °C for subsequent polymerization experiments.

Immobilization of Metallocene Catalysts on Nanoparticles. In the glovebox, 2.0 g of Al_2O_3 encapsulated nanoparticles, 200 mg of the metallocene precatalyst $EBIZrCl_2$, and 50 mL of toluene were loaded into a predried 200 mL flip-frit reaction flask. The color of the particle suspension turned to light orange. The slurry mixture was again subjected to alternating sonication and

(20) Pangborn, A. B.; Giardello, M. A.; Grubbs, R. H.; Rosen, R. K.; Timmers, F. J. *Organometallics* **1996**, *15*, 1518–1520.
(21) Neubrand, A.; Linder, R.; Hoffmann, P. *J. Am. Ceram. Soc.* **2000**, *83*, 860–864.
(22) Yoon, M.-H.; Kim, C.; Facchetti, A.; Marks, T. J. *J. Am. Chem. Soc.* **2006**, *128*, 12851–12869.
(23) (a) Chua, Y. T.; Stair, P. C. *J. Catal.* **2000**, *196*, 66. (b) Chua, Y. T.; Stair, P. C.; Wachs, I. E. *J. Phys. Chem. B* **2001**, *105*, 8600.

Scheme 2

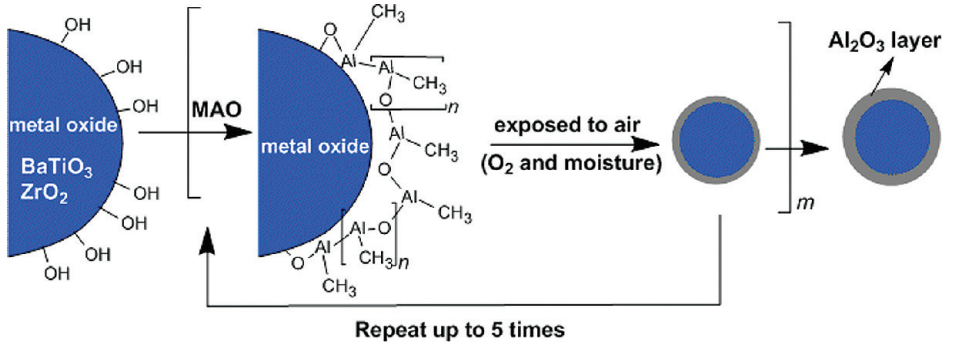

vigorous stirring overnight. The particles were then collected by filtration and washed with fresh toluene until the color of the toluene remained colorless. The particles were dried on the high-vacuum line overnight and stored in the glovebox at −40 °C in the dark.

Representative Synthesis of Nanocomposites via in situ Propylene Polymerization. In the glovebox, a 250 mL round-bottom three-neck Morton flask, equipped with a large magnetic stirring bar, was charged with 50 mL of dry toluene, 200 mg of the above catalyst-functionalized nanoparticles, and 50 mg of MAO. The assembled flask was removed from the glovebox and the mixture was subjected to sonication and vigorous stirring for 30 min. The flask was then attached to a high vacuum line (10^{-5} Torr), the catalyst slurry was degassed, equilibrated at the desired reaction temperature using an external water bath, and saturated with 1.0 atm (pressure control using a mercury bubbler) of rigorously purified propylene while vigorously stirring. After a measured time interval (changing the interval results in different particle loadings), the polymerization was quenched by the addition of 5 mL of methanol, and the reaction mixture was then poured into 800 mL of methanol. The composite was allowed to fully precipitate overnight and was then collected by filtration, washed with fresh methanol, and dried on the high vacuum line at 80 °C overnight to constant weight.

Results

I. Synthesis of Al_2O_3 Encapsulated $BaTiO_3$ and ZrO_2 Nanoparticles. Previous studies with $BaTiO_3$[24] and ZrO_2[25] nanoparticles revealed that different concentrations of hydroxyl groups are present on the surfaces of the two types of nanoparticles. The nanoparticle surfaces can be modified to form hydrophobic layers by reacting the surface hydroxyl groups with a surfactant, thus enhancing dispersion in nonpolar organic matrices.[26] In the present case, MAO reacts with the surface hydroxyl groups on the nanoparticles to form covalent Al−O bonds, thereby anchoring the MAO to the nanoparticle surfaces. After washing off excess MAO and exposure to air, the MAO on the nanoparticles surface rapidly oxidizes/hydrolyzes to form a shell of Al_2O_3. Depending on the size and surface properties of the nanoparticle, the thickness of the Al_2O_3 derived from a layer of MAO coating

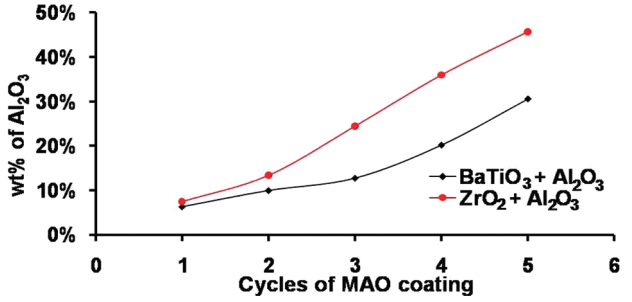

Figure 1. Wt % of Al_2O_3 on the $BaTiO_3$ or ZrO_2 nanoparticles as a function of the number of MAO deposition cycles n (n = 1−5), calculated from ICP data of the encapsulated nanoparticles.

varies slightly. In the present study, the MAO is applied multiple times to incrementally increase the Al_2O_3 shell thickness (Scheme 2). This process was monitored by ICP analysis (Figure 1), which shows that the Al_2O_3 layer content increases monotonically with an increase in the number of MAO coating cycles, and reaches about 10 nm thickness for $BaTiO_3$ and 7 nm thickness for ZrO_2 after 5 cycles, as is also evident in the TEM images (Figure 2). The thickness of Al_2O_3 on the particle types is slightly different because of the difference in the surface hydroxyl concentration and the size of the nanoparticles themselves.

The core-shell structures were confirmed by comparison of the TEM images for the pristine nanoparticles and the particles after the 5 coating cycles (Figure 2). For example, uniform Al_2O_3 layers with a thickness of approximately 10 nm are observed for the sample $BaTiO_3$−Al_2O_3(5) [this notation has the format, nanoparticle identity-aluminum oxide(number of layers)] after the coating process. XRD patterns of the coated nanoparticle samples (Figure 3) are found to be very similar to those of the pristine nanoparticles, indicating that the Al_2O_3 layers are essentially amorphous and that minimal Al ions are incorporated into the $BaTiO_3$ and ZrO_2 nanoparticle lattices during the coating process. UV Raman spectroscopy confirms that the Al_2O_3 is amorphous[27] since a sample of $BaTiO_3$−Al_2O_3(5) exhibits only features between 500 and 2000 cm^{-1} assignable to $BaTiO_3$ nanoparticles of this size (see spectra in Supporting Information Figure S1).[28]

(24) (a) Noma, T.; Wada, S.; Yano, M.; Suzuki, T. *J. Appl. Phys.* **1996**, *80*, 5223–5233. (b) Wad, S.; Narahara, M.; Hoshina, T.; Kakemoto, H.; Tsurumi, T. *J. Mater. Sci.* **2003**, *38*, 2655–2660.
(25) Zhao, Q.; Wang, X.; Cai, T. *Appl. Surf. Sci.* **2004**, *225*, 7–13.
(26) Chang, S.-J.; Liao, W.-S.; Ciou, C.-J.; Lee, J.-T.; Li, C.-C. *J. Colloid Interface Sci.* **2009**, *329*, 300–305.
(27) Xiong, G.; Elam, J. W.; Feng, H.; Han, C. Y.; Wang, H.-H.; Iton, L. E.; Curtiss, L. A.; Pellin, M. J.; Kung, M.; Kung, H.; Stair, P. C. *J. Phys. Chem. B* **2005**, *109*, 14059–14063.
(28) Yan, T.; Shen, Z.-G.; Zhang, W.-W.; Chen, J.-F. *Mater. Chem. Phys.* **2005**, *98*, 450–455.

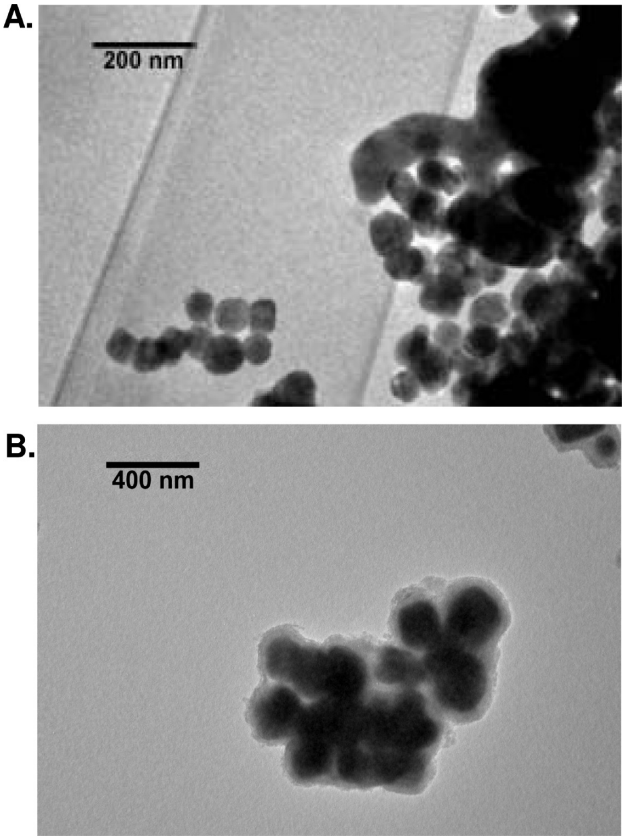

Figure 2. TEM images of pristine $BaTiO_3$ nanoparticles (A) and core-shell $BaTiO_3-Al_2O_3(5)$, $BaTiO_3$ nanoparticles with a thick Al_2O_3 layer coated with 5 cycles of MAO deposition (B). The different contrast in the image reveals a homogeneous layer of essentially amorphous Al_2O_3 on the surfaces of $BaTiO_3$ nanoparticles. Similar phenomena are observed for ZrO_2 and Al_2O_3 encapsulated nanoparticles (TEM and XRD in Supporting Information, Figures S2 and S3).

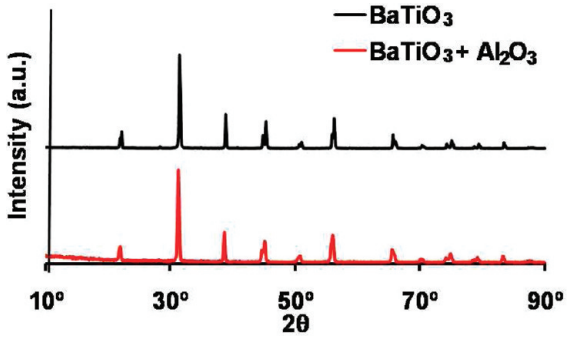

Figure 3. θ-2θ XRD scans of pristine $BaTiO_3$ nanoparticles and of $BaTiO_3$-nanoparticles coated with 5 cycles of MAO-derived Al_2O_3 shells.

II. Synthesis of Metal Oxide-Polypropylene Nanocomposites. The Al_2O_3 encapsulated nanoparticles discussed above were exposed to solutions of the metallocene precatalyst $EBIZrCl_2$, forming supported polymerization-active surface species. Subsequent in situ polymerization of propylene yields the corresponding core-shell nanoparticle-polyolefin nanocomposites. These nanocomposites consist of three intimately dispersed components: ceramic high-ε nanoparticles, medium-ε Al_2O_3 shells, and low-ε isotactic polypropylene. By controlling the polymerization time, $BaTiO_3-Al_2O_3(5)-^{iso}PP$ and $ZrO_2-Al_2O_3(5)-^{iso}PP$ [this notation has the format, nanoparticle identity-aluminum oxide(number of layers)-polymer matrix] nanoparticle volume fractions (including alumina layer) can be varied from 0.005 to 0.25.

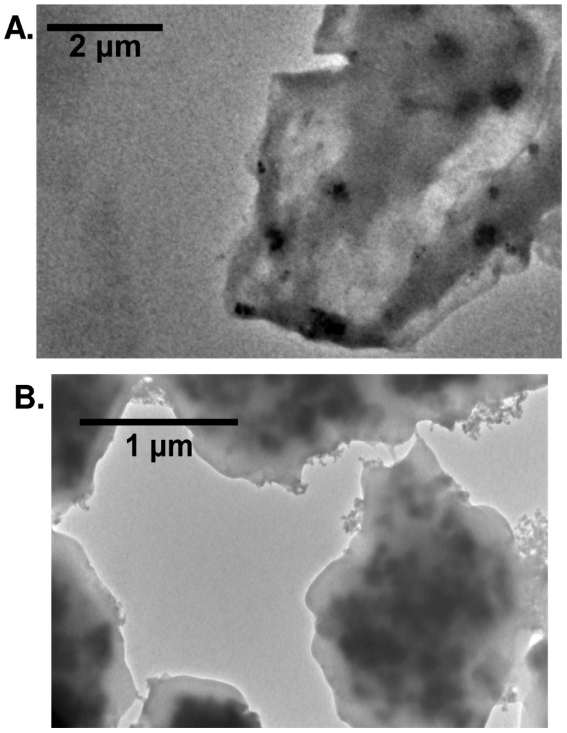

Figure 4. Representative TEM images of (A) $BaTiO_3-Al_2O_3(5)-^{iso}PP$ (ν_f 0.02) and (B) $ZrO_2-Al_2O_3(5)-^{iso}PP$ (ν_f 0.07) nanocomposites. The dark spheres are nanoparticles that are dispersed, and embedded in the irregular continuous matrix is the polymer.

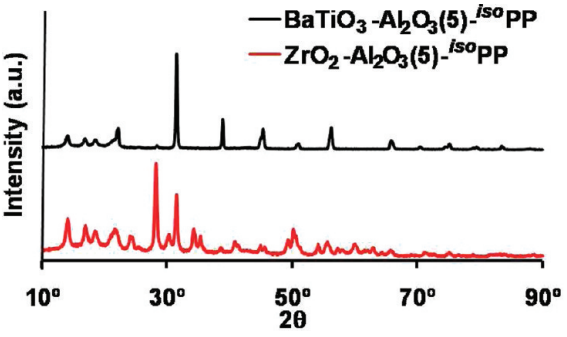

Figure 5. Representative θ-2θ XRD scans of $BaTiO_3-Al_2O_3(5)-^{iso}PP$ (ν_f 0.02) and $ZrO_2-Al_2O_3(5)-^{iso}PP$ (ν_f 0.07) nanocomposites. The low angle reflections are due to crystalline polypropylene.

As shown in a previous study, the C_2-symmetric metallocene catalyst $EBIZrCl_2$ (Chart 1) produces highly isotactic ([*mmmm*] = 83%) and crystalline (monoclinic α phase) polypropylene.[11] During the in situ polymerization process, the growing polyolefin chains produce very high local hydrostatic pressures, which help disrupt nanoparticle agglomeration and afford homogeneously dispersed ceramic nanoparticles in a polypropylene matrix. TEM images of the $BaTiO_3$ and ZrO_2 polypropylene nanocomposites (Figure 4) clearly show that the nanoparticles are embedded and dispersed in the polymer matrix. Generally, samples with lower nanoparticle loadings have better dispersion. The XRD θ-2θ scans for the nanocomposite (Figure 5) reveal the diffraction of crystalline

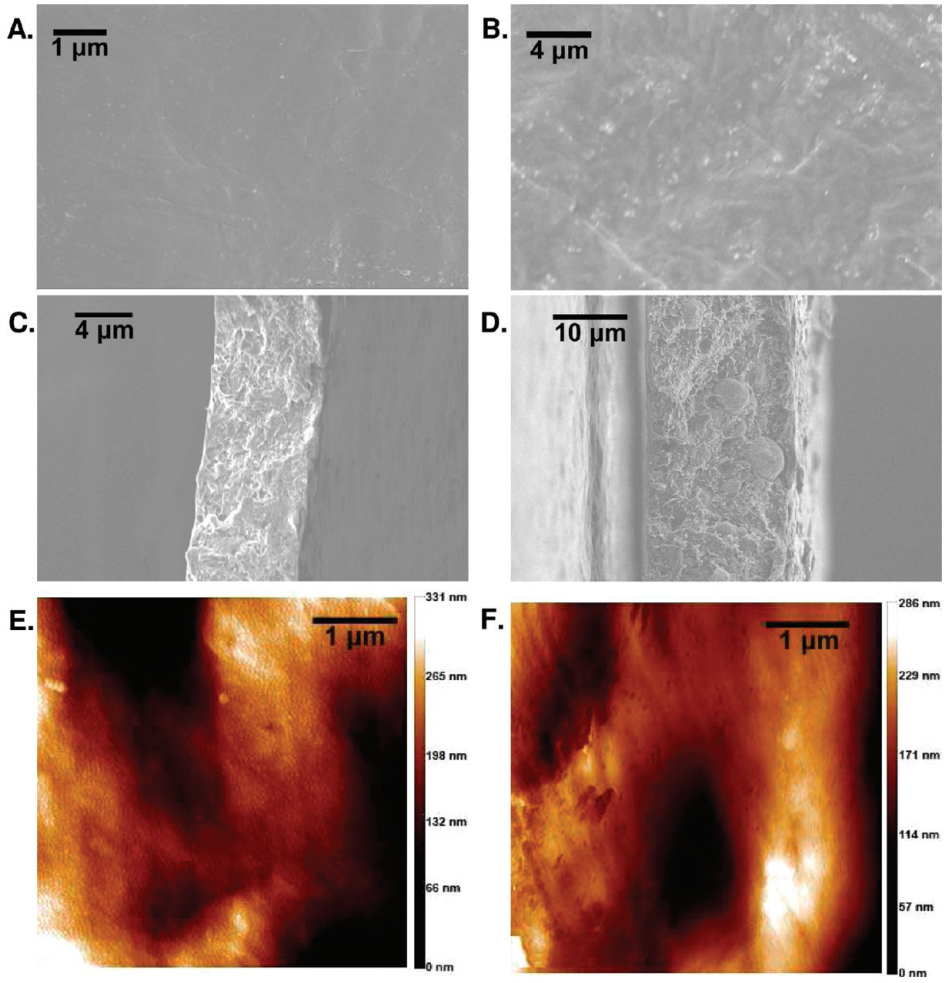

Figure 6. Sample surface and cross-sectional SEM images and AFM topographic images of nanocomposite thin films fabricated by hot-pressing. (A), (C), (E) $BaTiO_3-Al_2O_3(5)-^{iso}PP$ (ν_f 0.09) with rms roughness 3.84 nm and (B), (D), (F) $ZrO_2-Al_2O_3(5)-^{iso}PP$ (ν_f 0.06) with rms roughness 3.05 nm.

isotactic polypropylene at low angles as well as signals from the nanoparticles.[11] The Zr in the $EBIZrCl_2$ catalyst or in any catalyst hydrolysis/oxidation products is below the ICP detection limits in the $BaTiO_3-Al_2O_3(1)-^{iso}PP$ nanocomposites, and thus has been neglected in the modeling and analysis.

Thermal analysis shows that the melting points of the present nanocomposites are in the range 135−145 °C range, increasing with nanoparticle loading.[15] Thin films of $BaTiO_3-Al_2O_3(5)-^{iso}PP$ and $ZrO_2-Al_2O_3(5)-^{iso}PP$ were fabricated on aluminum substrates by hot-pressing at 130 °C under 1500 psi of pressure. For particle volume fractions greater than 0.15, it is difficult to fabricate uniform, high-quality films. The films with lower nanoparticle loadings are optically transparent; as loadings increase the films become more opaque. The morphology of the films was examined by SEM and AFM, and representative images are shown in Figure 6. Parallel-plate capacitors containing these nanocomposites were fabricated by vapor deposition of 50 nm gold electrodes on top of the hot-pressed films and were used to characterize the electrical and dielectric properties.

III. Nanocomposite Permittivity Properties. (*1*). *Effect of Filler Volume Fraction*. Effective permittivity data for the nanocomposites derived from capacitance measurements are compiled in Table 1. Generally, for $BaTiO_3-Al_2O_3(5)-^{iso}PP$ and $ZrO_2-Al_2O_3(5)-^{iso}PP$ nanocomposites, the effective permittivity increases as the filler volume fraction increases. Note that filler refers to the ceramic particle along with any Al_2O_3 shell. Composite permittivity increases slowly at lower loadings and then more rapidly above volume fractions near 0.05, and peaks at volume fractions around 0.13. Composites having a single layer of Al_2O_3 nanoparticle coating exhibit similar trends in permittivity versus volume fraction of filler. The permittivity of the nanocomposites decreases for volume loadings greater than 0.16. Previous studies have suggested that at high filler loadings, dielectric permittivity may decrease because of imperfect filler packing and that there is some agglomerization of the nanofiller, consequently a decrease in the total effective interfacial area between the filler and polymer matrix, thereby reducing the interfacial polarization.[29]

(*2*). *Maxwell−Garnett* (*MG*) *Effective Medium Theory*. For spherical inclusions, the effective permittivities of composites can be described using the Maxwell−Garnett

(29) (a) Afzal, A. B.; Akhtar, M. J.; Nadeem, M.; Hassan, M. M. *Curr. Appl. Phys.* **2010**, *10*, 601–606. (b) Ben, A. I.; Rekik, H.; Kaddami, H.; Raihane, M.; Arous, M.; Kallel, A. *J. Electrostat.* **2009**, *67*, 717–722.

Table 1. Dielectric Properties Data for Metal Oxide-Polypropylene Nanocomposites Having Different Al_2O_3 Shell Thicknesses on the Nanofillers

composite	total nanofiller[a] vol %[a]	ceramic vol %[b]	permittivity[c]	composite	total nanofiller[a] vol %[b]	permittivity[c]
$BaTiO_3$−MAO(5)−^{iso}PP	0.5%	0.4%	2.3 ± 0.3	$BaTiO_3$−MAO(1)−^{iso}PP	0.9%	3.1 ± 1.2
	2%	1%	2.7 ± 0.5		3%	2.7 ± 0.2
	4%	2%	2.8 ± 0.3		5%	2.9 ± 1.0
	7%	5%	3.5 ± 0.7		7%	5.1 ± 1.7
	13%	9%	6.0 ± 1.1		14%	6.1 ± 0.9
	24%	16%	3.7 ± 0.6			
ZrO_2−MAO(5)−^{iso}PP	0.4%	0.2%	2.5 ± 0.3	ZrO_2−MAO(1)−^{iso}PP	2%	1.7 ± 0.3
	2%	1%	2.6 ± 0.9		4%	2.0 ± 0.4
	4%	2%	2.6 ± 0.5		8%	4.8 ± 1.1
	10%	6%	3.1 ± 0.6		9%	5.1 ± 1.3
	13%	7%	6.2 ± 0.7			
	25%	14%	4.0 ± 0.5			

[a] Nanofiller indicates both ceramic and Al_2O_3 shell (Note: for single-layer Al_2O_3 samples, the vol % nanofiller is the same as the ceramic vol %). [b] From elemental analysis. [c] Derived from capacitance measurements.

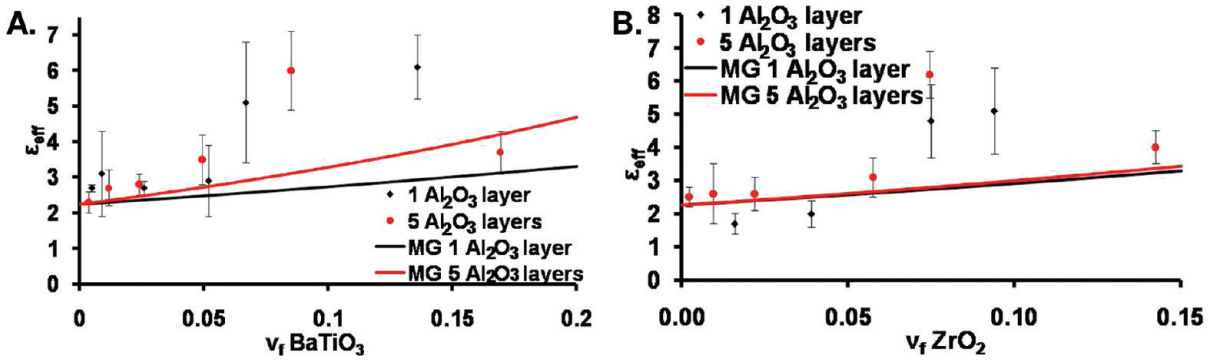

Figure 7. Comparison of MG theory and experimental effective permittivities for $BaTiO_3$−$Al_2O_3(n)$−^{iso}PP (A) and ZrO_2 −Al $_2O_3(n)$− ^{iso}PP nanocomposites (B).

(MG) effective medium theory (eq 1),[15,30] where ε_1 is the relative

$$\varepsilon_{eff} = \varepsilon_2 \frac{\varepsilon_1 + 2\varepsilon_2 + 2v_f(\varepsilon_1 - \varepsilon_2)}{\varepsilon_1 + 2\varepsilon_2 - v_f(\varepsilon_1 - \varepsilon_2)} \quad (1)$$

permittivity of the inner layer filler, ε_2 is the relative permittivity of the outer layer matrix, and v_f is the volume fraction of the inner layer. As shown in previous work, the present in situ polymerization approach for these types of core-shell nanocomposites is highly effective in disrupting the nanoparticle agglomeration, and therefore MG is a pragmatically acceptable model for describing the permittivity of these systems.[15]

In the nanocomposite systems discussed here, three layers are combined to create the bulk dielectric: ceramic nanoparticle, Al_2O_3, and isotactic polypropylene are introduced in that order. Thus, the MG equation is used twice; once for the nanoparticle with the Al_2O_3 coating to calculate the effective permittivity of the core-shell structure. Next, the ceramic-Al_2O_3 particles are regarded as the inner layer suspended in the polymer matrix to calculate an effective permittivity for the entire composite. Note that unless explicitly expressed, the volume fractions discussed are the volume fractions of ceramic in the system.

It can be seen in Figure 7 that the experimental permittivity data parallel MG theory for low volume fractions (Figure 7). However, they deviate from MG theory when the v_f is greater than ~0.06. That is, the experimental permittivities increase more rapidly than that predicted by MG theory and then after, v_f ~0.16, fall below that predicted by MG theory. The volume fraction where the permittivity falls below the predicted values corresponds approximately to volume fractions past the percolation threshold, as noted by others.[31] The increased permittivities over the MG-predicted values for volume fractions between 0.06 and 0.16 appear to reflect space charge[29] or percolation[30] effects. Others have attributed this rise and then fall in the permittivity to the effect of vacancies in the films because of imperfect mixing;[16] however, these effects, should be minimal in the present samples (as seen in Figure 6), and other mechanisms must be considered.

The present polypropylenes in the nanocomposites are highly crystalline (Figure 5), and when polymer encloses the nanoparticles, the polymer regions closest to the nanoparticle surfaces are expected to be less crystalline than the bulk polymer.[32] This can lead to structural defects in the polymer chains causing charge traps that have been previously attributed to space charge.[33] As the volume fraction of particles increases, the volume of polymer that

(30) Yang, R.; Qu, J.; Marinis, T.; Wong, C. P. *IEEE Trans. Compon. Packag. Technol.* **2000**, *23*, 680–683.
(31) Shen, Y.; Lin, Y.; Li, M.; Nan, C. W. *Adv. Mater.* **2007**, *19*, 1418–1422.
(32) Fornes, T. D.; Paul, D. R. *Polymer* **2003**, *44*, 3945–3961.
(33) Takada, T.; Hayase, Y.; Tanaka, Y. *IEEE Trans. Dielectr. Electr. Insul.* **2008**, *15*, 152–160.

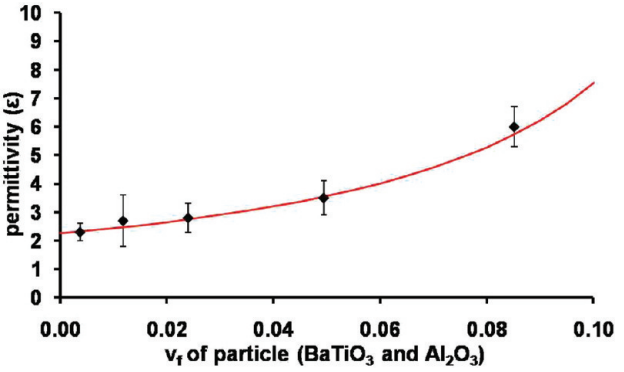

Figure 8. Experimental permittivity for $BaTiO_3-Al_2O_3(5)-^{iso}PP$ and least-squares-fit to eq 2 with $v_c = 0.16$ and $q = 0.61$. A graphical exponential fit to find parameter q is shown in the Supporting Information Figure S5.

occupies the less crystalline regions increases, and thus the number of charge traps should increase, leading to higher space charge densities.[29]

At high volume fractions, the average distance between nanoparticles is smaller, and the polymer expanse separating the nanoparticles becomes thinner, which will ultimately cause the composite to behave like a percolative system.[34] According to polymer composite percolation theory, the permittivity for conductor−insulator composites having a high matrix−filler dielectric contrast follows a volume fraction power law and exhibits an abrupt decline past the percolation threshold.[30] The general theory predicts the effective permittivity before the percolation threshold is given in eq 2, where ε_m is the permittivity of the matrix, v_f is the filler volume

$$\varepsilon_{eff} = \varepsilon_m \left| \frac{v_c - v_f}{v_c} \right|^{-q} \qquad (2)$$

fraction, v_c is the percolation threshold, and q is a critical exponent.[35] If the inclusion phase particles are spherical and similar in size to the matrix phase, then a random distribution of inclusions will have a percolation threshold at ~16 vol %.[36] Large filler particle sizes and nanoparticle agglomerization can result in a lower percolation threshold.[37] The variation of experimental permittivity for $BaTiO_3-Al_2O_3(5)-^{iso}PP$ nanocomposites can be fit to the percolation law with $v_c = 0.16$, resulting in $q = 0.61$ (Figure 8). Since simple MG theory does not account for either space charge or percolation effects, and percolation theory can only account for the $BaTiO_3$ trends, a more sophisticated model must be derived to account for these experimentally observed trends.

(34) (a) Gonon, P.; Boudefel, A. *J. Appl. Phys.* **2006**, *99*, 024308. (b) Qi, L.; Lee, B. I.; Chen, S.; Smuuels, W. D.; Exarhos, G. J. *Adv. Mater.* **2005**, *17*, 1777–1781. (c) Xu, J. W.; Wong, C. P. *Appl. Phys. Lett.* **2005**, *87*, 082907. (d) Pecharromán, C.; Moya, J. S. *Adv. Mater.* **2000**, *12*, 294–297. (e) Fisch, F.; Harris, A. B. *Phys. Rev. B* **1978**, *18*, 416–420.
(35) Grannan, D. M.; Garland, J. C.; Tanner, D. B. *Phys. Rev. Lett.* **1981**, *46*, 375–378.
(36) (a) Dang, Z. M.; Lin, Y. H.; Nan, C. W. *Adv. Mater.* **2003**, *15*, 1625–1629. (b) Nan, C. W. *Prog. Mater. Sci.* **1993**, *37*, 1–116.
(37) (a) Huang, X. Y.; Jiang, P. K. *J. Appl. Phys.* **2007**, *102*, 124103. (b) Dutton, R. E.; Rahaman, M. N. *J. Mater. Sci. Lett.* **1993**, *12*, 1453–1456.

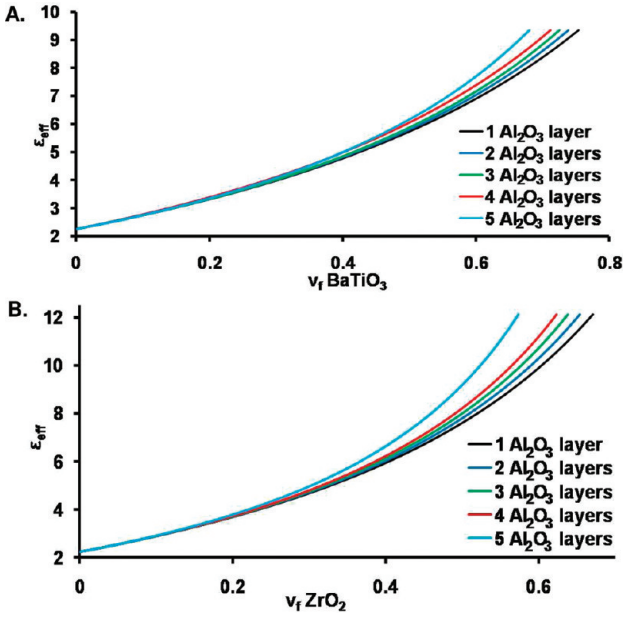

Figure 9. MG-derived effective permittivity as a function of the volume fraction of the indicated filler for (A) 140 nm diameter $BaTiO_3$ and (B) 70 nm diameter ZrO_2 nanoparticles with the indicated numbers of Al_2O_3 layers coating the nanoparticles.

(*3*). *Effect of Al_2O_3 Layer Thickness.* To elucidate the effect of the Al_2O_3 shell layer thickness on the effective permittivities of the present nanocomposites, we compare the samples with one to five layers of MAO-derived Al_2O_3 coating. At a low volume fraction of ceramic nanoparticles in the total dielectric, the composites with thicker Al_2O_3 layers have permittivities that are slightly greater than those with only a single Al_2O_3 layer. Increased numbers of Al_2O_3 layers represents a substitution of some of the polypropylene with Al_2O_3 which has a higher permittivity, and thus the effective nanocomposite permittivity increases.

MG theory was also applied to model the data from samples having different numbers of Al_2O_3 layers. As seen in Figure 9, upon increasing the thickness of the Al_2O_3 shells, the effective permittivity increases marginally. On $BaTiO_3$ particles, which have an average radius of 70 nm, each layer of Al_2O_3 is about 2 nm thick, as calculated from ICP-derived elemental composition. On the ZrO_2 particles, with an average radius of 35 nm, each Al_2O_3 layer is about 1.4 nm thick.

(*4*). *Frequency Dependence of Permittivity.* The capacitances of the $BaTiO_3-Al_2O_3(5)-^{iso}PP$ and $ZrO_2-Al_2O_3(5)-^{iso}PP$ nanocomposite films were also characterized as a function of frequency (Figure 10). In the 100 Hz to 1 MHz range, the dielectric permittivity increases as the nanoparticle loading increases until the loading reaches the critical 0.16 volume fraction, at which point the permittivity falls, consistent with the observations presented above. For the samples with low nanoparticle loadings, the dielectric permittivities vary little with frequency while the samples with higher nanoparticle loadings exhibit falling dielectric permittivity at higher frequencies. Lower permittivity at higher frequencies indicates greater space charge and has been observed for other polymer-ferroelectric

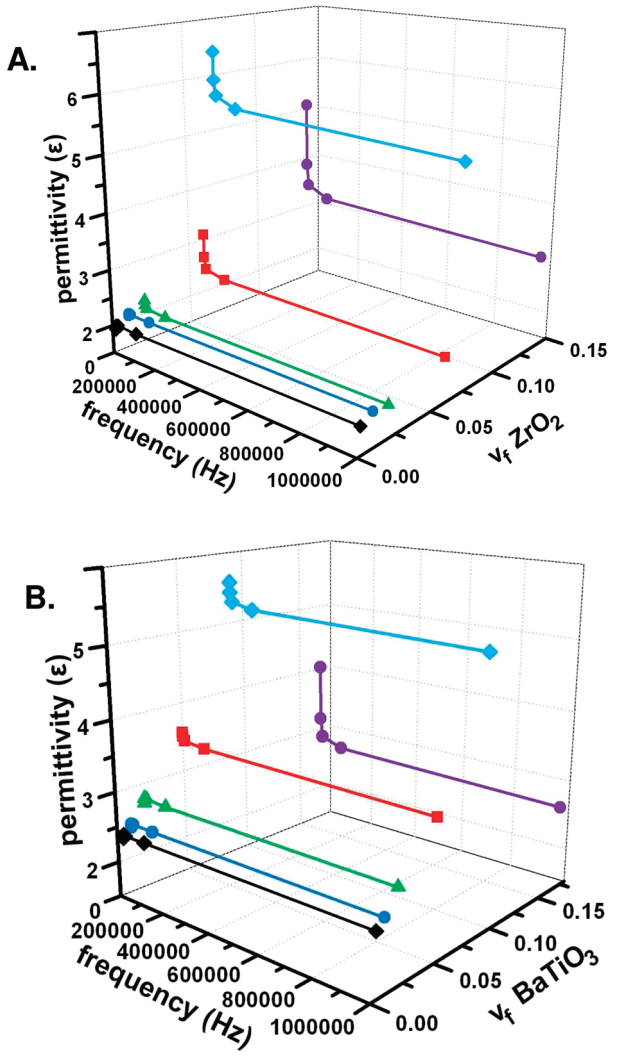

Figure 10. Frequency-dependent dielectric response of capacitors fabricated from $BaTiO_3-Al_2O_3(5)-^{iso}PP$ (A) and $ZrO_2-Al_2O_3(5)-^{iso}PP$ (B) nanocomposites.

ceramic composites.[38] For representative samples, the capacitance was also measured as a function of temperature at various frequencies (Supporting Information Figure S6). For a given frequency, the dielectric permittivities decline only slowly with increasing temperature, falling only ~5% from 25 to 90 °C.

IV. Dielectric Loss. (*1*). *Effect of Filler Concentration.* Figure 11 shows the dielectric loss for capacitors fabricated from $BaTiO_3-Al_2O_3(5)-^{iso}PP$ and $ZrO_2-Al_2O_3(5)-^{iso}PP$ nanocomposites. With a thick Al_2O_3 coating on the nanoparticle surfaces, the losses are significantly suppressed, particularly for the samples having low nanoparticle concentrations at high frequency. The dielectric loss increases significantly as the nanoparticle volume fraction increases. For a given sample, the loss decreases with increasing frequency in the range 100 Hz to 1 MHz.

(*2*). *Effect of Al_2O_3 Shell Thickness.* Ideally in a capacitor, dielectric losses should be as low as possible. Although all of the present $BaTiO_3-Al_2O_3(n)-^{iso}PP$ nanocomposites generally exhibit low dielectric loss (less than 0.01 at

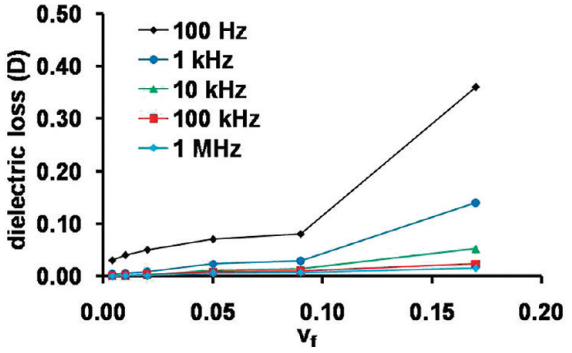

Figure 11. Frequency-dependent dielectric loss for capacitors fabricated from $BaTiO_3-Al_2O_3(5)-^{iso}PP$ nanocomposites.

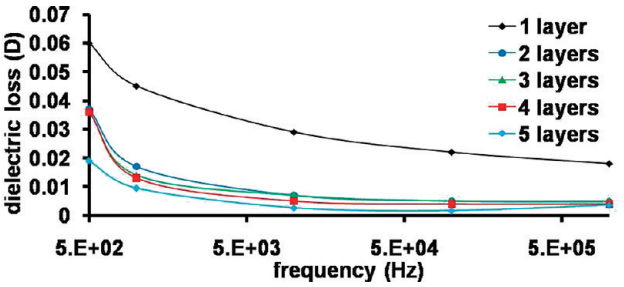

Figure 12. Comparison of dielectric loss for capacitors fabricated from $BaTiO_3-Al_2O_3(n)-^{iso}PP$ nanocomposites, $n = 1-5$. The nanoparticle volume fractions are ~0.07.

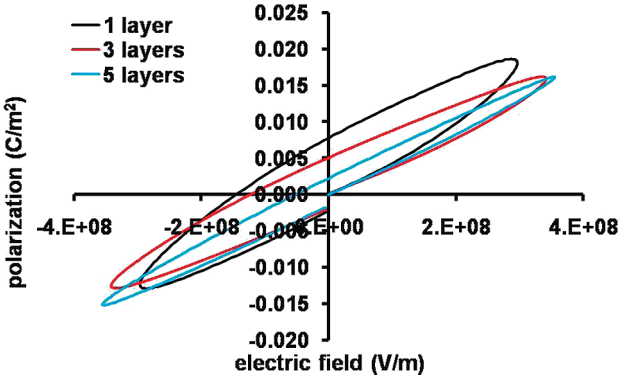

Figure 13. Electric field-polarization loops for $BaTiO_3-Al_2O_3(n)-^{iso}PP$ nanocomposites $n = 1, 3, 5$. The volume fractions of $BaTiO_3$ are 0.05, 0.08, and 0.09 for $n = 1$, 3, and 5, respectively.

1 kHz), the loss clearly decreases for samples with increasing numbers of MAO-derived Al_2O_3 layers (Figure 12). Each sample exhibits dielectric loss that decreases slightly with increasing frequency, consistent with the permittivity data for these samples ($\nu_f < 0.09$) which show little dependence on frequency (see Figure 10). For samples at fixed frequency, the dielectric loss exhibits little temperature dependence over the range 30 to 90 °C (Supporting Information Figure S8). To determine nanocomposite dielectric loss at high fields, sample polarization was measured as a function of electric field. Polarization response "loops" (Figure 13) can be related to the energy capacity and loss, where energy storage, U_e, is related to the field of the polarization loop just before break-

$$U_e = \varepsilon\varepsilon_0 E^2 \quad (3)$$

(38) Popielarz, R.; Chiang, C. K.; Nozaki, R.; Obrzut, J. *Macromolecules* **2001**, *34*, 5910–5915.

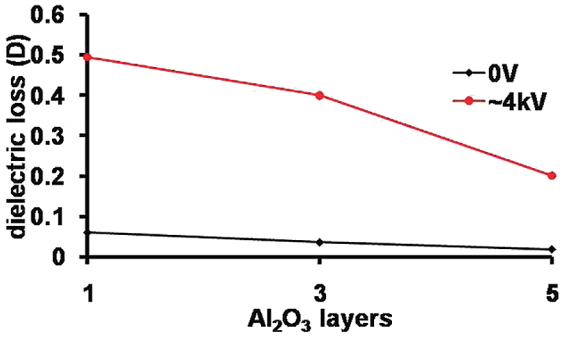

Figure 14. Comparison of dielectric loss for capacitors fabricated from $BaTiO_3$−$Al_2O_3(n)$−^{iso}PP nanocomposites, n = 1, 3, 5 Al_2O_3 layers at low and high field. The volume fractions of $BaTiO_3$ are 0.05, 0.08, and 0.09 for n = 1, 3, and 5, respectively.

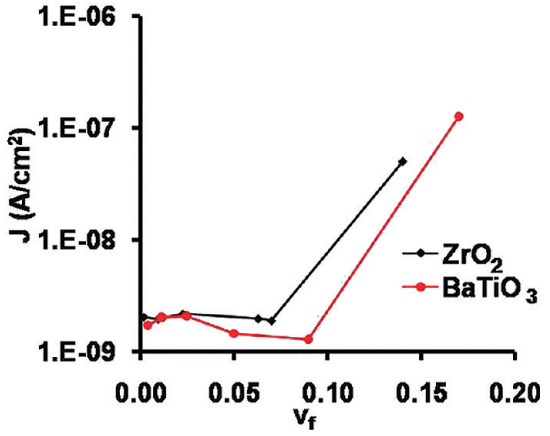

Figure 15. Leakage current density at 100 V for $BaTiO_3$−$Al_2O_3(5)$−^{iso}PP and ZrO_2−$Al_2O_3(5)$−^{iso}PP nanocomposites having different volume of nanoparticle loadings.

down, E, the dielectric constant of the system, ε, and the vacuum permittivity, ε_o (eq 3). The high field loss can be found by the ratio of energy density recovered and the energy stored (eq 4, this can be seen graphically in the Supporting Information Figure S9). At high fields (4 kV), the dielectric loss is 10× greater

$$D = \frac{U_{lost}}{U_{stored}} = \frac{U_{stored} - U_{regained}}{U_{stored}} \qquad (4)$$

than that at low fields (Figure 14); however, in both cases the loss decreases markedly as the Al_2O_3 shell thickness is increased.

V. Leakage Current Density. The leakage current densities of the present nanocomposite films with low nanoparticle volume fractions ($\nu_f < 0.10$) are generally within the range 10^{-8}−10^{-9} A/cm^2 in an applied electric field of 10^5 V/cm (Figure 15). At the low loading levels ($\nu_f < 0.10$), the leakage currents are so small that the differences between the different loadings are within the instrumental uncertainty. Thus, there is no discernible correlation between leakage current and nanoparticle volume fraction, and the present nanocomposites are all excellent insulators. However, for samples with the highest nanoparticle loadings (ν_f nanoparticle > 0.16), the leakage current density increases substantially, presumably because of imperfect filler packing, agglomerization of the nanofiller, and/or percolation. For $\nu_f < 0.12$, the leakage current density and dielectric loss remain very low while the permittivity increases approximately 3-fold at ν_f just above 0.09, yielding the best performing capacitors of the series.

Discussion

I. Synthesis of Al_2O_3 Encapsulated Core-Shell Nanoparticles and Polypropylene Nanocomposites. Al_2O_3-encapsulated $BaTiO_3$ and ZrO_2 nanoparticles having core-shell structures can be efficiently synthesized by repeated contact with an MAO solution. In each coating cycle, the nanoparticles are surrounded by chemisorbed polymeric organoaluminum species, MAO, which when oxidized/hydrolyzed yields a layer of amorphous Al_2O_3 about 2 nm thick. This layer-by-layer deposition approach has several advantages over conventional spray-coating and thermolysis methods[39] for preparing inorganic core/shell nanoparticles. First, the coating layer is covalently bound to the surface of the nanoparticles; the bonding is robust and avoids shell separation from the core. Also, the thickness of the coating layer can be controlled by the number of coating cycles. Finally, this process affords a uniform coating layer.

The metallocene precatalyst is next chemisorbed/activated by the MAO layer on the surface of these core/shell particles, and subsequent in situ olefin polymerization affords the corresponding nanocomposites. It is known that nanoparticle agglomerization and phase separation between hydrophilic metal oxides and hydrophobic polymers can compromise nanocomposite electrical properties, resulting in increased leakage current and local dielectric breakdown.[40] The pathway of the present in situ coordinative polymerization process is such that the propagating polymer chains efficiently disrupt the nanoparticle agglomerization and afford good nanoscale dispersion as indicated by SEM and TEM images. The pronounced homogeneity of the nanocomposites is also confirmed by the uniformity of the films (SEM) fabricated by hot-pressing and by the low surface rms roughnesses achieved (AFM), while nanocomposite films prepared by simple mixing of the two constituents typically exhibit large cracks, voids, and pinholes.[9b] Adding surfactant during composite processing can improve the dispersion and the film quality; however, residual free surfactant can also lead to high leakage currents and dielectric loss,[40] both of which are not an issue for the present materials.

II. Effect of Al_2O_3 Layer on Nanocomposite Properties. Ceramic metal oxides such as $BaTiO_3$ with a permittivity of greater than 2000, have large permittivity contrasts with polypropylene, which has a permittivity of 2.25. For

(39) (a) Li, D.; Kato, Y.; Kobayakawa, K.; Noguchi, H.; Sato, Y. *J. Power Sources* **2006**, *160*, 1342–1348. (b) Kim, Y.; Kim, H. S.; Martin, S. W. *Electrochim. Acta* **2006**, *52*, 1316–1322. (c) Miyashiro, H.; Kobayashi, Y.; Seki, S.; Mita, Y.; Usami, A.; Nakayama, M.; Wakihara, M. *Chem. Mater.* **2005**, *17*, 5603–5605.
(40) Cho, S. -D.; Paik, K. -W. *IEEE Electron. Compon. Technol. Conf.* **2001**, 1418–1422.

Scheme 3. Dielectric Composite Structural Motifs: (A) High Permittivity Sphere in a Low Permittivity Matrix, (B) High Permittivity Sphere in a Low Permittivity Matrix with a Buffer Layer of Medium Permittivity between Them, and (C) Sphere Where the Matrix Permittivity Is Graded from Center to Edge

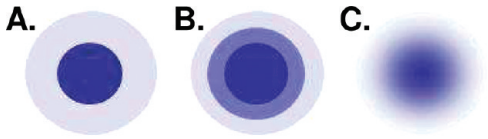

directly dispersed ceramic nanoparticles in polypropylene,[3] the very large contrasts in relative permittivities between host and guest result in a large disparity in the electric fields within the constituent phases,[41] which will induce discontinuous variations in the local electric field at the interfaces, and adversely affect the bulk dielectric properties. Ideally, composites having graded permittivities where the permittivity decreases gradually from the center of the particle to the border (Scheme 3c), should minimize this effect. Inclusion of core-shell nanoparticles (Scheme 3b) having a shell permittivity between that of the core and polymer matrix affords a realistic model to study the effects of permittivity contrast on nanocomposite dielectric properties. This approach complements research on interfacial layer effects on laminated insulators.[42]

In the present materials, the Al_2O_3 ($\varepsilon \sim 10$) shell on the nanoparticles acts as a dielectric buffer between the high permittivity $BaTiO_3$ and ZrO_2 nanoparticles and the polypropylene matrix. With a 10 nm thick Al_2O_3 coating on $BaTiO_3$ (5 layers), the leakage and the dielectric loss are greatly reduced. Leakage and dielectric loss not only cause dissipation of energy but also produce undesired thermal effects in the film. Coating Al_2O_3 on the nanoparticle inclusions offers an efficient, cost-effective approach to minimizing these adverse effects. Along with other recent advances in inorganic core-shell nanoparticles,[43] we expect that further work on encapsulated nanoparticles as fillers in polymer matrixes will afford practical routes to even higher performing dielectric materials.

III. Effective Medium Models. Effective medium models are commonly used to estimate effective permittivities for simple systems having spherical dielectric inclusions embedded in a host material.[44] Here we generalize to the case of encapsulated nanoparticle fillers by first calculating the effective permittivity of the core-shell structure, treating the core filler within the shell, and then treating the entire core-shell structure as the filler in the polymer matrix. The theoretical calculations evidence good agreement with the experimental permittivity values when the filler concentrations are relatively low ($\nu_f < 0.06$). At higher nanoparticle loadings, the permittivity is better described by a percolation power law for the $BaTiO_3$ nanocomposites but not for those of ZrO_2.

Conclusions

In this study, we report an effective layer-by-layer method for creating Al_2O_3 shells on the surfaces of high-ε $BaTiO_3$ and ZrO_2 nanoparticles. The coating layer is covalently bonded to the surface of the nanoparticles, and the thickness of the coating layer can be incrementally controlled by the number of MAO coating cycles. The metallocene precatalyst $EBIZrCl_2$ is chemisorbed and activated by these Al_2O_3-encapsulated nanoparticles having core/shell structures. In situ polymerization of propylene by the catalysts anchored on these core-shell nanoparticles then affords nanocomposites with the filler well-dispersed in the polyolefin matrix. The moderate permittivity of the Al_2O_3 layer greatly suppresses leakage currents and dielectric loss in these nanocomposite materials. Such nanocomposites, with high permittivity, small dielectric loss, and small dependence of permittivity and dielectric loss on temperature, are attractive for physically small capacitors with large energy storage capacities and high rating voltages.

Acknowledgment. This research was supported by the ONR MURI Program (N00014-05-1-0766), DOE (Grant 86ER13511), and made use of Central Facilities supported by the NSF MRSEC program (DMR-0520513) at the Materials Research Center of Northwestern University. The SEM and TEM analyses were performed in the EPIC facility of the NUANCE Center at Northwestern University. We thank Dr. N. Guo for helpful discussions, Prof. H. Mohseni and Mr. W. Wu for assistance with the LCR meter, and Ms. S. L. Wegener for help in acquiring UV-Raman Spectra.

Supporting Information Available: Corresponding ZrO_2 data not included in this main text. Also temperature dependent data including permittivity and dielectric loss are included, along with graphical representations of loss calculations and percolation theory fitting. This material is available free of charge via the Internet at http://pubs.acs.org.

(41) (a) Percharroman, C.; Moya, J. S. *Adv. Mater.* **2000**, *12*, 294–297. (b) Pham Thi, M.; Velasco, G.; Colomban, P. *J. Mat. Sci. Lett.* **1986**, *5*, 415–417.

(42) (a) Tewari, P.; Rajagopalan, R.; Furman, E.; Lanagan, M. T. *J. Colloid Interface Sci.* **2009**, *332*, 65–73. (b) Lee, B. H.; Jeon, Y.; Zawadzki, K.; Qi, W. J.; Lee, J. *Appl. Phys. Lett.* **1999**, *74*, 3143–3145.

(43) (a) Joo, S. H.; Park, J. Y.; Tsung, C.-K.; Yamada, Y.; Yang, P.; Somorjai, G. A. *Nat. Mater.* **2009**, *8*, 126–131. (b) Galian, R. E.; de la Guardia, M.; Perez-Prieto, J. *J. Am. Chem. Soc.* **2009**, *131*, 892–893. (c) Cheng, Y. C.; Liu, X. H.; Guo, J. J.; Liu, F.; Li, Z.; Xu, G.; Cui, P. *Nanotechnology* **2009**, *20*, 055604. (d) Song, Y. Y.; Cao, X. B.; Guo, Y.; Chen, P.; Zhao, Q.; Shen, G. Z. *Chem. Mater.* **2009**, *21*, 68–77.

(44) (a) Maldovan, M.; Bockstaller, M. R.; Thomas, E. L.; Carter, W. C. *Appl. Phys. B: Laser Opt.* **2003**, *76*, 877–884. (b) Busch, K.; Soukoulis, C. M. *Phys. Rev. Lett.* **1995**, *75*, 3442–3445.